

Simultaneous Monitoring of Molecular Thin Film Morphology and Crystal Structure by X-ray Scattering

Nada Mrkyvkova,* Peter Nadazdy, Martin Hodas, Jianwei Chai, Shijie Wang, Dongzhi Chi, Michaela Sojkova, Martin Hulman, Andrei Chumakov, Oleg V. Konovalov, Alexander Hinderhofer, Matej Jergel, Eva Majkova, Peter Siffalovic, and Frank Schreiber



Cite This: *Cryst. Growth Des.* 2020, 20, 5269–5276



Read Online

ACCESS |



Metrics & More

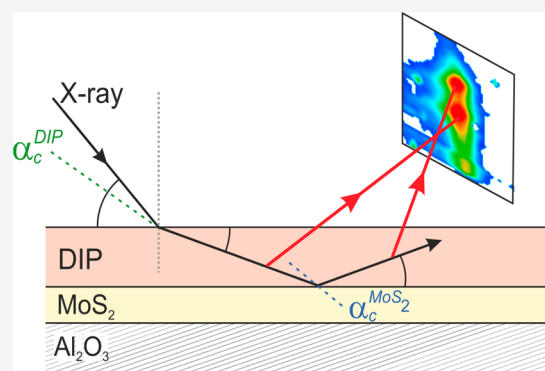


Article Recommendations



Supporting Information

ABSTRACT: Hybrid materials of π -conjugated molecular semiconductors combined with two-dimensional (2D) materials exhibit a significant potential for novel (opto)electronics. The overall characteristics of molecular growth, such as molecular packing, crystallographic structure, and morphology, determine the specific application. The growth studies are thus key for understanding and improving these systems. So far, a *simultaneous* real-time study of the thin film morphology evolution along with its crystalline phase on a 2D substrate has not been performed. Here, we report on an additional feature of surface-sensitive grazing-incidence wide-angle X-ray scattering (GIWAXS). We show that refraction induced multiple scattering effects can be employed to reveal the morphology-related growth modes of a thin organic layer on a 2D underlayer together with the crystallographic structure and molecular orientation. A thorough description of the dynamic scattering effects is provided, allowing a detailed study of the Bragg peak splitting in the out-of-plane direction. We discuss the influence of the material-related parameters, such as stress and growth type, on the mutual position of the split peaks during the growth. Furthermore, we show that the time-resolved GIWAXS enables the observation of the electron density variation in real time. Our findings should be considered as a general feature of GIWAXS that can be applied to various types of thin films, where the temporal evolution of morphology, molecular arrangement, and crystallographic structure are of interest.



1. INTRODUCTION

Thin films composed of small π -conjugated molecules have already been successfully used in various organic-based devices.^{1–3} Their versatility also causes an emerging interest in the field of pharmaceutical research^{4,5} and neuroscience.⁶ The morphology, molecular packing, and crystallographic structure of these films are of fundamental importance for their charge transport and optical properties.^{7–12} However, various factors (stress/strain, grain boundaries, etc.) can affect the molecular orientation and the crystalline structure throughout the layers,^{13–15} influencing the overall properties of the organic film. Knowledge of the thin film properties during growth is thus important from the application point of view but can be difficult to acquire experimentally. At the same time, understanding the mechanisms underlying the growth of these systems is very challenging also from a theoretical perspective, in particular, in terms of their inherent anisotropy and orientational degrees of freedom.^{16–18}

For small organic molecules, the molecular arrangement and morphology are often closely related, meaning that the morphology of the thin film can indirectly reveal the molecular orientation.^{19–21} The morphology can be observed directly,

using various types of scanning-probe microscopies such as atomic force microscopy (AFM), scanning electron microscopy (SEM), etc. These techniques typically probe just the surface of the layer or have only limited penetration depth. Consequently, to track the film properties with increasing the film thickness, many *ex-situ* scans at different thicknesses are required. This approach might not always be possible, e.g., in the case of strongly oxidizing surfaces or other types of postgrowth changes, and *real-time in situ* techniques are more suitable. Real-time experiments are of high relevance since they allow observation of the transient, nonequilibrium phenomena during the growth. Among many different real-time techniques focused on the morphology determination, such as low-energy electron microscopy (LEEM) or Auger spectroscopy,^{22,23} X-ray diffraction methods are well established. One of the

Received: April 2, 2020

Revised: June 23, 2020

Published: June 29, 2020



advantages of diffraction techniques is their nonlocal character of the probe, where the examined area can be on the order of several square millimeters, ensuring statistically relevant results. They also allow structural studies spanning many length scales, from the atomic scale up to several hundreds of nanometers.²⁴ The morphology and the growth modes in soft-matter systems were studied by specular X-ray reflectivity (XRR) and grazing-incidence X-ray techniques, mainly grazing-incidence small-angle X-ray scattering (GISAXS).^{24–27}

In this paper, we show that the multiple scattering effects in grazing-incidence wide-angle X-ray scattering (GIWAXS) can be exploited for in situ and real-time studies of basic growth modes, in addition to the molecular packing and crystallographic structure in thin films. The multiple scattering inside the studied layer leads to a splitting of the diffraction peaks in grazing-incidence geometries. This effect is mainly observed in GISAXS, where the scattered wave amplitude consists of four terms.²⁸ In GISAXS, the multiple-scattering effects (requiring *dynamical theory*) can be employed to determine the symmetry of the nanoparticles on flat surfaces.^{29,30} On the other hand, the dynamic scattering approach inherent for refractive media³¹ is not widely used in GIWAXS, although the refractive index of the layer can strongly influence the position of the diffraction peaks. Unlike GISAXS, only two scattering channels are realized at large exit angles in GIWAXS geometry, as indicated in Figure 1 (peaks L and U). The first channel originates from the scattering of the primary X-ray beam in the thin film, while the second one is driven by the scattering of the totally reflected X-ray beam at the thin film/substrate interface.^{32,33} This refraction-induced feature in the diffraction pattern was theoretically well described within the dynamical theory of X-ray diffraction; however, it has remained largely unused for practical purposes up to now.

Here, we report on the Bragg-peak splitting in a diffraction pattern measured in the thin layer of diindenoperylene (DIP) molecules by GIWAXS. The peak splitting is observed for the incident X-ray angles between the critical angles of DIP film and the underlying MoS₂ substrate. Furthermore, we thoroughly investigate the time-evolution of both scattering channels of a selected Bragg diffraction during DIP growth. From the analysis of their time-evolution, we are able to determine the respective growth modes of the organic layer for two distinct MoS₂ substrates. We believe that this paper extends the applicability of GIWAXS, and the presented results will find use in real-time morphology determination for a large variety of materials.

2. EXPERIMENTAL SECTION

The MoS₂ monolayer was grown on *c*-plane Al₂O₃ substrates, using magnetron sputtering of Mo target in vaporized sulfur ambient. The MoS₂ growth was performed at a substrate temperature of 700 °C, with a sulfur partial pressure of 4.0×10^{-7} mbar, and a processing gas (Ar) pressure of 6.0×10^{-4} mbar. The sputtering power was kept very low at 6 W, which enabled extremely slow growth to create a MoS₂ monolayer. The thickness of the MoS₂ layer was controlled by the growth time, and the quality of the MoS₂ film was confirmed by Raman spectroscopy, measuring the distance between the E_{2g} and A_{1g} peaks.^{34,35} The 9 nm thick MoS₂ substrate having its *c* crystallographic axis parallel to the substrate was prepared by a one-zone CVD sulfurization of a 3 nm thick Mo layer on *c*-plane Al₂O₃ substrates.³⁶ The sulfurization took place in an inert N₂ atmosphere, with a sulfur temperature of 800 °C. DIP powder was purchased from the Institute of Physics, University of Stuttgart (Stuttgart, Germany). The DIP films were prepared by organic molecular beam deposition

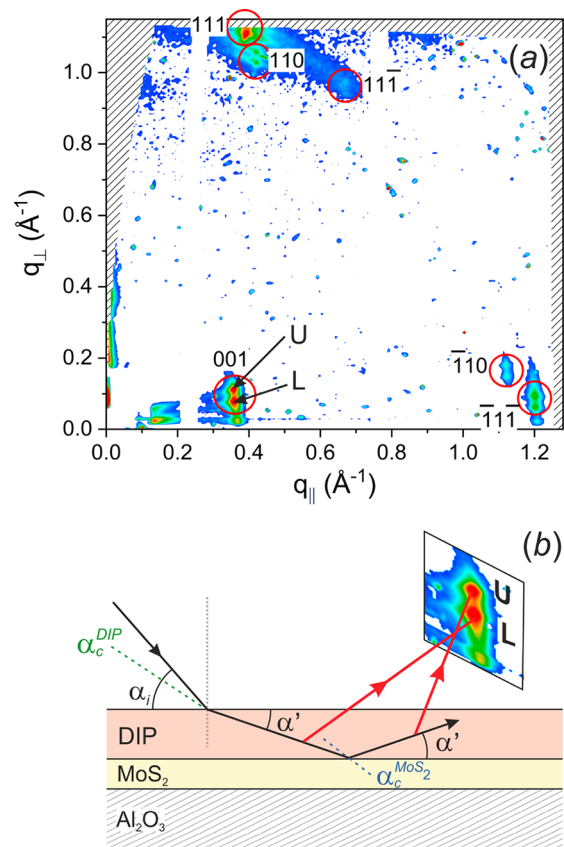


Figure 1. (a) GIWAXS pattern of the 12 nm thick DIP layer grown on MoS₂ monolayer (intensity increasing from blue to red). The Bragg diffractions from (001), (110), (111), (110), (111), and (111) crystallographic planes are denoted in red circles. The peaks U and L represent the upper and lower part of the split 001 diffraction peak, respectively (see main text for details). (b) Schematic representation of the two key scattering pathways. α_i is the angle of incidence and α' is the angle of refraction for X-rays. α_c^{DIP} and $\alpha_c^{\text{MoS}_2}$ are the critical angles of DIP layer and MoS₂ layer, respectively. The red arrows indicate the diffracted beams in the DIP layer.

(OMBD)^{16,17} in a vacuum chamber ($p \approx 2 \times 10^{-8}$ mbar). The DIP powder was heated up to 250 °C (evaporation rate ~ 1.0 Å/min) and deposited onto the MoS₂ substrates. The substrates were kept at a constant temperature of 50 °C during the whole deposition. We note that prior to the actual deposition, the substrates were annealed at 320 °C to desorb any surface contaminants. The *effective* thickness was monitored during the DIP growth by a quartz crystal microbalance (QCM). The *effective* thickness measured by QCM was calibrated from the ex-situ thickness calibration of DIP films on Si wafer by the spectroscopic ellipsometry (J. A. Woolam, M-2000V) prior to the DIP deposition on MoS₂ layers. The *effective* thickness indicates the thickness of the DIP film grown on an amorphous surface (e.g., silicon with native oxide) with a standing-up molecular orientation. More details on the preparation procedure are provided in ref 34. The GIWAXS measurements were performed at the ESRF/ID10 beamline (Grenoble, France) and also using a laboratory source (Excillum, MetalJet X-ray Source). In all experiments, the energy of the X-ray beam was 9.25 keV ($\lambda = 1.34$ Å), and the angle of incidence was predominantly set to $\alpha_i = 0.2^\circ$. At the synchrotron, the total flux of the X-ray beam was attenuated to 10^{10} photons/s, which was found to be below the damage threshold of the molecular film for a beam size of $\sim 17 \times 200 \mu\text{m}^2$. Under laboratory conditions, the beam flux was lower by 2 orders of magnitude with the beam size of $\sim 1 \text{ mm}^2$. In order to measure in situ GIWAXS, the DIP growth took place in a custom-built OMBD chamber equipped with a 360° cylindrical beryllium window, enabling the detection of wide-angle diffraction.³⁷

The GIWAXS patterns were collected by a hybrid-pixel detector (Dectris, Pilatus 300 K) with 320 μm thick Si sensor. The AFM measurements (Bruker, DimensionEdge) were performed utilizing silicon probes (Bruker, TESPA-V2) in tapping mode.

3. RESULTS AND DISCUSSION

Figure 1a shows the reciprocal space map of DIP layer grown on the MoS₂ monolayer measured in the GIWAXS geometry (see Figure S1 in the Supporting Information). The Bragg peaks originating from distinct crystallographic planes are visible regardless the sample azimuth, which is a consequence of the fiber texture of DIP crystallites.³⁴ An evident splitting of all Bragg peaks can be observed for the incident angle $\alpha_i = 0.2^\circ$. Apart from the Bragg peaks, a weak horizontal line of enhanced diffuse scattering is visible at $q_{\perp} \approx 0.028 \text{ \AA}^{-1}$, known as the Yoneda peak,³⁸ with the most pronounced intensity for the 001 and $\bar{1}\bar{1}\bar{1}$ diffractions. The angular position of the Yoneda peak coincides well with the critical angle of the DIP film ($\alpha_c^{\text{DIP}} \approx 0.15^\circ$ for $\lambda = 1.34 \text{ \AA}$).^{39,40} No diffraction peak originating from the MoS₂ monolayer is visible in Figure 1a. In the detected reciprocal area, only the 002 diffraction would be observable ($q \approx 1 \text{ \AA}^{-1}$). However, in the case of a monolayer, there is only one diffraction diffracting plane with its *c*-axis perpendicular to the substrate's plane, and thus no diffraction can be seen.

The peak splitting in Figure 1a can be explained by taking into account dynamical scattering effects inherent to grazing-incidence X-ray diffraction^{31,32,41} as schematically shown in Figure 1b. The lower (L) peak of the peak doublet originates directly from the Bragg scattering of the primary X-ray beam refracted in the DIP layer. The refracted beam is further totally reflected at the DIP/MoS₂ interface, as the incident angle of the refracted beam α' is smaller than the critical angle of the total reflection $\alpha_c^{\text{MoS}_2}$ (we expect that the critical angle given by the complex refractive index is similar for the MoS₂ monolayer and bulk). The subsequent Bragg scattering of the totally reflected beam in the DIP layer gives rise to the upper (U) diffraction peak. The splitting of the peaks is given solely by the refractive index change and acts on the vertical component q_{\perp} (direction normal to sample surface) of the scattering vector exclusively, so the in-plane component of the scattering vector q_{\parallel} is the same for the upper and lower peak. The most pronounced effect of the refraction is thus the shift of the peaks toward higher q_{\perp} (see eq 1). The reciprocal space positions of the lower diffraction peaks were utilized directly to determine the crystallographic structure of the thin organic layers,^{34,42–44} often omitting the refraction correction.³³ On the other hand, the evaluation of the upper diffractions is more complicated as their position in the q_{\perp} direction is strongly influenced by the incident angle of the primary X-ray beam; see Figure 2.

Figure 2 shows the positions of the lower (L) and upper (U) 001 diffraction peaks depending on the incident angle of the X-ray beam (α_i). The precise positions of L and U in the q_{\perp} direction were obtained by fitting the peaks with a Gaussian function. Clearly, the α_i -dependence of both peaks is different. Peak L is almost independent of α_i , whereas the position of peak U increases with the increasing α_i . We were able to track the position of the upper peak only for $\alpha_i \leq 0.4^\circ$, as its intensity decreases rapidly for $\alpha_i > \alpha_c$ according to Fresnel's law;^{31,45} see inset in Figure 2. This confirms the fact that the upper diffraction peak involves reflection on the MoS₂ substrate, for which the diffracted intensity decreases strongly with increasing the incident angle. In order to analyze the α_i -

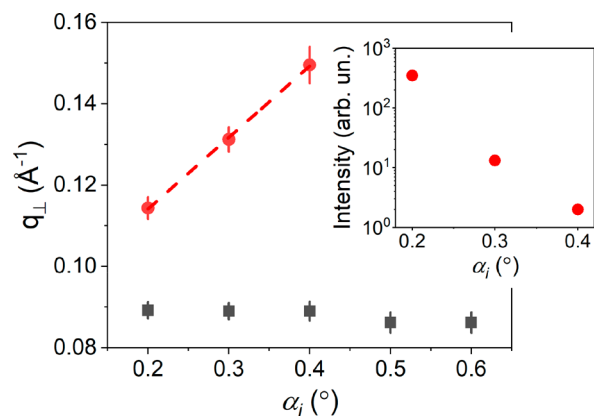


Figure 2. Reciprocal space positions (out-of-plane component) of the lower (black) and upper (red) 001 diffraction peaks as a function of the incident beam angle α_i . The red dashed line is a fit with a slope proportional to the used X-ray wavelength. The inset shows the intensity dependence of the upper 001 diffraction peak on α_i in logarithmic scale.

dependence of peaks L and U in more detail, we write the perpendicular components (q_{\perp}) of their positions in reciprocal space as follows:

$$q_L = q_{0L} + \Delta q_L \quad (1a)$$

$$q_U = q_{0L} + \Delta q_U \quad (1b)$$

where q_{0L} is the position of the Bragg peak when refraction can be neglected ($n_{\text{DIP}} = 1$). The offsets Δq_L and Δq_U from the unperturbed q_{0L} include the refraction effect and refraction/reflection effects, respectively. Employing Bragg's equation and Taylor expansion for small angles, we obtain (see Supporting Information for derivation):

$$\Delta q_L = \frac{2\pi}{\lambda}(\alpha_i - \alpha') \quad (2a)$$

$$\Delta q_U = \frac{2\pi}{\lambda}(\alpha_i + \alpha') \quad (2b)$$

where λ is the wavelength of the primary X-ray beam and α' is the incident angle after the refraction as defined in Figure 1b. Equation 2 shows that in the case of no refraction ($\alpha_i = \alpha'$), the lower diffraction is independent of α_i , and the upper diffraction is proportional to α_i with a proportionality constant of $4\pi/\lambda$. The measured angular dependence of the 001 diffraction peak positions on the incident angle shown in Figure 2 is validated by eq 2. The fitted slope for the upper diffraction matches the used X-ray wavelength. A slight decrease in the L peak position for larger α_i is a consequence of the refractive index of the DIP layer (n_{DIP}) being smaller than 1 (for more details, see ref 33).

In the following section, we will study the movement of the two 001 diffraction peaks in reciprocal space during organic film growth (with α_i being set to 0.2°). We will demonstrate that their evolution can vary significantly, depending on the growth type and/or film morphology. Figure 3a shows the reciprocal space positions of L and U peaks for increasing DIP thickness. The points in Figure 3a were obtained by fitting both diffraction peaks separately in the q_{\parallel} and q_{\perp} directions. As mentioned earlier, the q_{\parallel} component of the L and U peaks is the same for arbitrary DIP thickness, and its absolute value is given by the length of the unit cell (UC) parameter c . In the

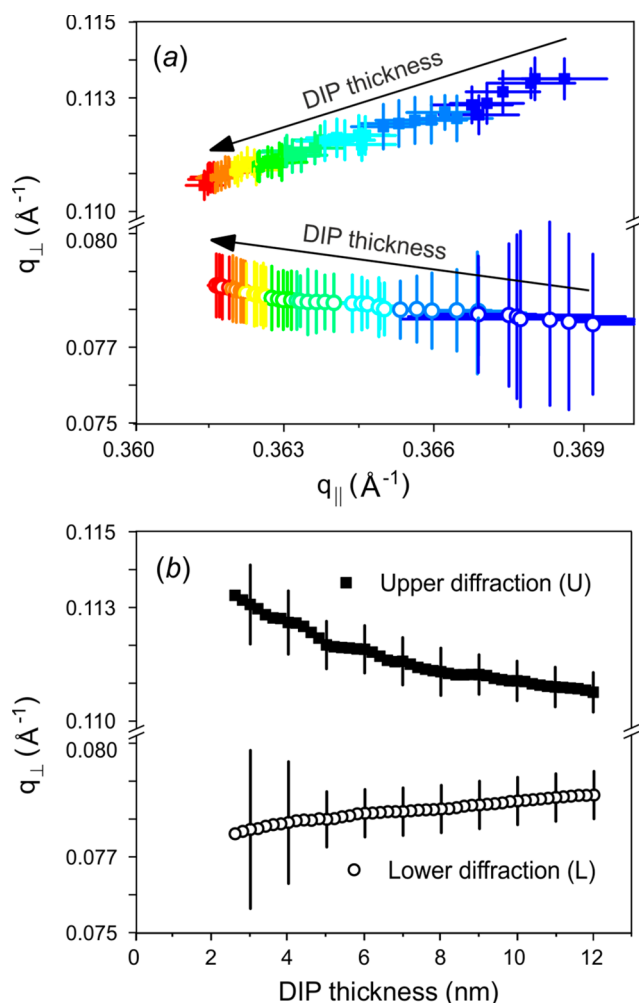


Figure 3. (a) Evolution of the 001 diffraction peaks L (open circles) and U (full squares) in reciprocal space during DIP growth. The arrows indicate the timeline of the growth, which corresponds to the increasing DIP thickness (color-coded from blue to red). (b) The equivalent evolution of the perpendicular component (q_{\perp}) of the peaks U and L as a function of DIP thickness.

case of the MoS₂ monolayer as a substrate, the DIP molecules are oriented almost in the lying-down fashion with the *c*-axis aligned along the long molecular axis.³⁴ Such a *lying-down* orientation gives rise to a nonzero q_{\parallel} component of 001 diffraction peak, in contrast to the *standing-up* orientation on weakly interacting substrates.^{21,26,39} The temporal change in the q_{\parallel} position visible in Figure 3a suggests the microscopic stress that will be discussed later. Since the peak splitting is independent of q_{\parallel} , Figure 3b shows the q_{\perp} position of L and U peaks as a function of the effective DIP thickness.¹⁹ In Figure 3b, the peaks could not be reliably fitted for the layer thicknesses below ~2.5 nm due to a low diffracted intensity at the beginning of the growth. Nevertheless, the distinct evolution of the q_{\perp} position for both diffraction peaks is obvious. The lower peak position is shifting toward larger q_{\perp} , whereas the upper peak position is decreasing with increasing the DIP thickness.

To explain such behavior, we have to consider all factors that determine the diffraction position (and might change during the growth). The first important factor is the refractive index of the organic layer, n_{DIP} , which gives rise to the spatial separation of the peaks. The spacing between the L and U diffraction

peaks $\Delta q_{\text{DIP}} = \Delta q_{\text{U}} - \Delta q_{\text{L}}$ is given by (see Supporting Information for derivation):

$$\Delta q_{\text{DIP}} = \frac{4\pi}{\lambda} \sin \alpha' \quad (3)$$

where α' is determined by n_{DIP} through Snell's law:

$$\cos \alpha' = \frac{1}{n_{\text{DIP}}} \cos \alpha_i \quad (4)$$

For X-rays, the real part of the refractive index slightly deviates from unity ($n_{\text{DIP}} = 1 - \delta$), where the deviation $\delta = \alpha_c^2/2$ is directly related to the scattering properties of the organic film, i.e., the electron density ρ_e . For small organic molecules, δ is typically on the order of 10^{-6} .^{33,46} Using Snell's law, eq 3 can be rewritten in the following form (see Supporting Information for derivation):

$$\Delta q_{\text{DIP}} = \frac{4\pi}{\lambda} \sin \alpha_i \left(1 - \frac{\delta}{\sin^2 \alpha_i} \right) \quad (5)$$

Note that this equation is valid for $\alpha_i \neq 0$, which is following the fact that the incoming X-ray beam will be reflected from the organic layer for $\alpha_i < \alpha_c^{\text{DIP}}$. Equation 5 confirms that the spatial separation of the two peaks is controlled by the refraction (n_{DIP} is given by δ). Moreover, it validates a constant spacing between the two peaks during the growth of a uniform organic layer (with a well-defined refraction index). However, for small organic molecules on 2D substrates, it was observed that instead of a closed uniform layer, in many cases, they tend to form separate islands on the surface of the substrate.^{34,47–49}

These islands, typical for the Volmer–Weber growth mode, create an inhomogeneous coverage of the substrate that cannot be described by a constant refractive index. More rigorously speaking, the molecular islands with unequal volumes should be described by a spatially varying effective permittivity, i.e., index of refraction. However, such a complicated environment can be simplified by introducing a gradient effective medium approach (originating from the Maxwell Garnett formula; see ref 50 for more details). In this model, the randomly distributed DIP islands are substituted by several closed DIP layers with spatially varying effective refractive index, $n_{\text{eff}}^{\text{DIP}}$, in the direction normal to the substrate. In such case, $n_{\text{eff}}^{\text{DIP}}$ can be defined as a linear function that decreases with increasing DIP thickness ($n_{\text{eff}}^{\text{DIP}} = 1 - \beta t$, where β is a material-related constant, and t represents DIP thickness or time). Such a description is valid until the DIP islands do not occupy the whole area of the substrate, forming a so-called closed layer with constant n_{DIP} . Using $n_{\text{eff}}^{\text{DIP}}$ in eq 5, we obtain that Δq_{DIP} decreases linearly with time (i.e., DIP thickness), meaning that the two diffractions, L and U, are moving toward each other symmetrically.

By careful examination of Figure 3b, one can notice that the experimental points do not approach symmetrically. The gradual increase of the lower diffraction is attenuated, whereas the upper diffraction decreases more rapidly. At this stage, we have to take into account the second important factor that influences the position of the diffraction peaks—the microscopic stress. The stress in the DIP layer can occur as a consequence of different surface energies of the underlying substrate and the organic layer itself. The main effect of the stress in the organic film is the change of the UC parameters (*c*-parameter in the case of 001 diffraction in our data), which will lead to a shift of the diffraction positions in the *q*-space. We note that in the case of the *c*-parameter change, the

diffraction spot would move along the line intersecting the origin of the reciprocal space defined by the primary X-ray beam. Most importantly, stress has the same influence on both studied diffractions. It means that regardless of the stress type, i.e., the unit cell evolution, the positions of the L and U diffractions will move simultaneously in the reciprocal space with increasing DIP thickness. Equation 3 confirms this statement directly, as α' is independent of θ . We would like to remark that both the crystallite size and strain contribute to the broadening of the observed diffraction peaks. However, a significant convolution of the illuminated sample surface with the diffracted peak width together with a small number of observed diffractions disables a quantitative determination of the crystallite size and strain. Moreover, the peak broadening was found to be the same for the L and U diffractions and is not involved in any of our calculations, which are based purely on the peak positions.

Combining the consequences of the growing layer morphology and UC changes on the L and U peak positions due to changes in the refractive index and stress, respectively, we can obtain the observed asymmetric evolution of the peak positions with increasing DIP thickness. Furthermore, the stress type—*tensile* or *compressive*—can be determined from a closer examination of the L and U peak evolution in Figure 3b. The tensile strain causes an extension of the UC parameters (see Figures S3, S4, and S5 in the Supporting Information), leading to a decrease of the q_{\perp} positions for L and U simultaneously. On the other hand, the compressive stress would increase the L and U positions because of the contraction of the UC parameters. Now, when combining these two scenarios with the opposing evolution of the L and U positions caused by the refractive index change, we can obtain a faster decrease of U and a slower increase of L for the *tensile* stress. This is in accordance with our recent findings of the strained DIP unit cell on few-layer MoS₂ substrates¹⁹ up to a layer thickness of about 15 nm. Here, we would like to point out the usefulness of choosing the 001 diffraction. Apart from the fact that this diffraction has the highest intensity, which allows tracking its evolution from the very thin DIP thickness, it encodes only the c -parameter of the UC (dominating in the q_{\parallel} direction for the lying-down molecular orientation). The 001 diffraction thus enables a straightforward interpretation of the c -parameter evolution during the DIP growth. Such an analysis would be more complicated for the diffraction peaks encoding more parameters of the UC.

Figure 4a shows the evolution of the L and U diffractions for the DIP layer up to a thickness of 62 nm. We note that the data in Figure 4a show larger error bars as they were measured in the laboratory (with less intense and broader beam, see Experimental Section), compared with the data shown in Figure 3, measured using the synchrotron radiation. The convergence of the L and U positions is symmetric (within the experimental error) along their average value $q_{\perp} \approx 0.096 \text{ \AA}^{-1}$ for the thicknesses ≥ 20 nm. The 20 nm is thus a *critical* DIP thickness where the stress saturates, and furthermore, the shift of the peaks is caused exclusively by the refractive index change. The laboratory conditions do not allow observation of the asymmetric diffraction evolution for the thicknesses below 20 nm because the intensity of the diffractions was too low. The critical thickness of ≈ 20 nm is, however, in good agreement with our previous observation of the stress saturation¹⁹ obtained by a different experimental approach. The observed continuous change of the refractive index

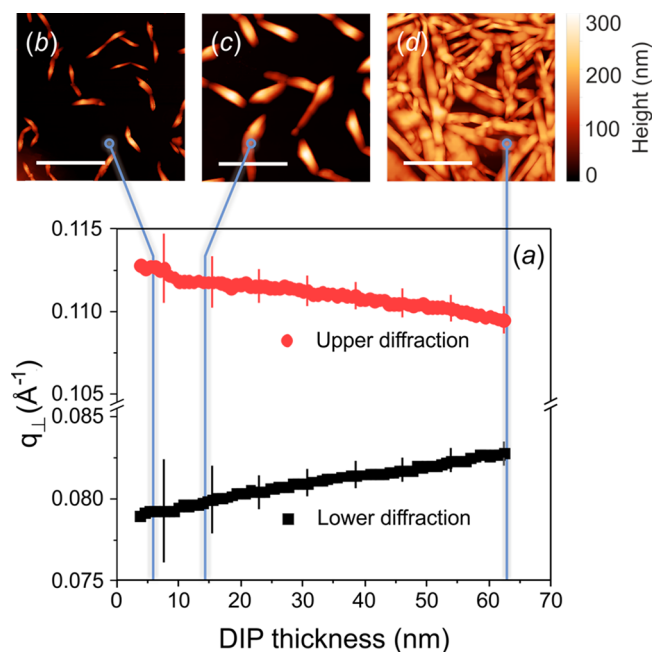


Figure 4. (a) Evolution of the L and U diffraction peaks along the q_{\perp} direction for DIP growth on the MoS₂ monolayer. AFM images of the DIP crystals for layers 6, 13, and 62 nm thick in (b), (c), and (d), respectively. The length of the scale bar is 2 μm .

suggests that the DIP layer has not been closed even for a thickness of 62 nm. The AFM images shown in Figure 4b–d confirm the 3D island growth (Volmer–Weber growth mode) for the *effective* DIP thicknesses of 6, 13, and 62 nm, respectively.

In the following, we will test our findings on the substrate that allows a closed layer formation with a constant n_{DIP} . Figure 5 shows the evolution of the lower and upper 001 peaks

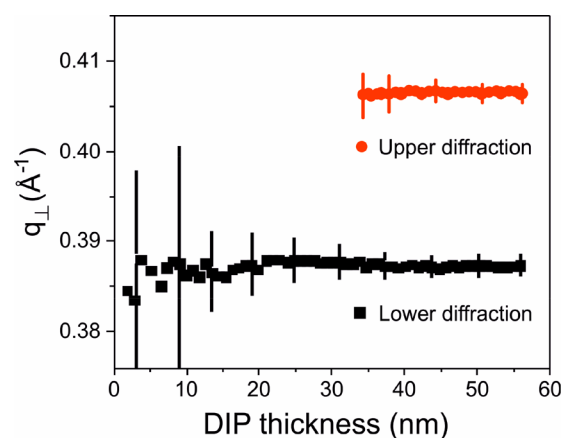


Figure 5. Evolution of the lower and upper split of the 001 diffraction for the standing-up molecules on a 9 nm thick MoS₂ underlayer.

of the DIP layer grown on 9 nm thick MoS₂ underlayer (see Figure S6 in the Supporting Information). It was observed that the thicker MoS₂ layers (MoS₂ thickness ~ 9 nm) with the c crystallographic axis aligned in the substrate plane support the growth of the *standing-up* phase of DIP layers.¹⁹ For the standing-up molecules, a layer-plus-island growth mode (Stranski–Krastranov growth mode)^{16,51} is typical (see Figure S7 in the Supporting Information), in contrast to the 3D island

growth for the lying-down molecules mentioned earlier in the text. Consequently, the formation of a closed layer occurs soon after a few DIP layers are grown.

The evolution of the lower and upper diffractions shown in Figure 5 suggests a constant n_{DIP} at least for the DIP thicknesses larger than 32 nm. The evolution of n_{DIP} for thicknesses smaller than 32 nm was impossible to track due to a low intensity in the upper diffraction. We can also conclude that the stress in the layer is fully saturated for thicknesses larger than 32 nm, as both diffractions evolve constantly with DIP thickness. Furthermore, Figure 5 provides directly a Δq_{DIP} value from which δ can be calculated using eq 5. The obtained value of $\delta \approx 3.9 \times 10^{-6}$ gives us the critical angle of the DIP layer $\alpha_c \approx 0.16^\circ$, which is in a good agreement with $\alpha_c = 0.15^\circ$ measured by specular X-ray reflectivity.^{39,40}

Here, we have shown that real-time GIWAXS gives access to the growth type and refractive index of a thin organic layer. In particular, the growth type can be associated with the spacing between L and U diffraction peaks during the growth. In principle, GIWAXS also enables determination of the electron density ρ_e (as δ is directly proportional to ρ_e) and its evolution during molecular growth. The electron density of a thin film is typically determined by X-ray reflectivity (XRR). XRR is sensitive to the electron density change in the direction perpendicular to the substrate plane but can only be applied in the case of low surface roughness comparable to the X-ray wavelength. The limitation imposed by the surface roughness excludes XRR studies in the case of the 3D island growth, where the size of the islands is on the order of tens of nanometers. GIWAXS can partially overcome this limitation, as it probes the electron density changes in all directions and does not inherently require a well-defined layer interface in contrast to XRR. This renders GIWAXS a multipurpose technique for the real-time studies of the thin (organic) layers, such as those exhibiting fiber-like (uniaxial) texture. It has a limited application for the nontextured layers displaying Bragg rings, as well for monocrystalline epitaxial layers. In summary, we have shown that the character of the split diffraction peak evolution during the organic film growth reveals the morphology of the layer indirectly. The constant spacing between the split diffractions during the growth suggests the Stranski–Krastanov growth mode, whereas the decreasing peak separation points to the Vonlner–Weber growth mode.

4. CONCLUSIONS

In the present work, we have studied the splitting of Bragg diffraction peaks from a growing thin diindenoperylene (DIP) film deposited on a MoS₂ substrate by grazing-incidence wide-angle X-ray scattering (GIWAXS). The observed peak splitting was explained as two separate scattering channels of the incident X-ray beam being formed in the thin organic layer. One of the channels originates from the Bragg scattering of the primary beam within the layer, and the other one arises as a consequence of the substrate-induced total beam reflection followed by a subsequent scattering on the same set of Bragg planes. Furthermore, we have studied the evolution of the split 001 diffraction in reciprocal space with increasing DIP thickness. We provide a simple mathematical description for their temporal evolution (i.e., evolution with increasing DIP thickness) in terms of the dynamical scattering theory. From the mutual evolution of the two scattering channels, we were able to determine the type of growth of the organic layer. For the MoS₂ monolayer substrate, the two diffraction spots move

toward each other in the q_{\perp} direction with increasing DIP thickness. This indicates an unclosed, 3D island growth of DIP molecules up to the thickness of 62 nm. The measured diffraction pattern of the DIP film also validated a lying-down orientation of the molecules. On the other hand, for the thicker MoS₂ layer, we observed a symmetric evolution of the diffraction peaks, suggesting the formation of a closed layer during the growth of standing-up molecules. Moreover, we determined the refractive index of the DIP layer from the GIWAXS reciprocal maps.

■ ASSOCIATED CONTENT

Supporting Information

The Supporting Information is available free of charge at <https://pubs.acs.org/doi/10.1021/acs.cgd.0c00448>.

Experimental GIWAXS setup, refraction correction for GIWAXS, time-evolution of the unit cell parameters, and DIP film on 9 nm thick MoS₂ layer (PDF)

■ AUTHOR INFORMATION

Corresponding Author

Nada Mrkyvkova – Institute of Physics and Centre for Advanced Materials Application, Slovak Academy of Sciences, Bratislava 84511, Slovakia; orcid.org/0000-0002-2619-0872; Email: nada.mrkyvkova@savba.sk

Authors

Peter Nadazdy – Institute of Physics, Slovak Academy of Sciences, Bratislava 84511, Slovakia

Martin Hodas – Institut für Angewandte Physik, Universität Tübingen, 72076 Tübingen, Germany; orcid.org/0000-0001-6328-1717

Jianwei Chai – Institute of Materials Research & Engineering (IMRE), A*STAR (Agency for Science, Technology and Research), Innovis, Singapore 138634

Shijie Wang – Institute of Materials Research & Engineering (IMRE), A*STAR (Agency for Science, Technology and Research), Innovis, Singapore 138634

Dongzhi Chi – Institute of Materials Research & Engineering (IMRE), A*STAR (Agency for Science, Technology and Research), Innovis, Singapore 138634; orcid.org/0000-0001-9562-1595

Michaela Sojkova – Institute of Electrical Engineering, Slovak Academy of Sciences, 845 11 Bratislava, Slovakia; orcid.org/0000-0002-7490-3240

Martin Hulman – Institute of Electrical Engineering, Slovak Academy of Sciences, 845 11 Bratislava, Slovakia; orcid.org/0000-0002-5598-9245

Andrei Chumakov – European Synchrotron Radiation Facility, Grenoble 38000, France

Oleg V. Kononov – European Synchrotron Radiation Facility, Grenoble 38000, France

Alexander Hinderhofer – Institut für Angewandte Physik, Universität Tübingen, 72076 Tübingen, Germany; orcid.org/0000-0001-8152-6386

Matej Jergel – Institute of Physics and Centre for Advanced Materials Application, Slovak Academy of Sciences, Bratislava 84511, Slovakia; orcid.org/0000-0002-4482-7881

Eva Majkova – Institute of Physics and Centre for Advanced Materials Application, Slovak Academy of Sciences, Bratislava 84511, Slovakia; orcid.org/0000-0001-9597-9247

Peter Siffalovic – Institute of Physics and Centre for Advanced Materials Application, Slovak Academy of Sciences, Bratislava 84511, Slovakia; orcid.org/0000-0002-9807-0810

Frank Schreiber – Institut für Angewandte Physik, Universität Tübingen, 72076 Tübingen, Germany

Complete contact information is available at:
<https://pubs.acs.org/10.1021/acs.cgd.0c00448>

Notes

The authors declare no competing financial interest.

ACKNOWLEDGMENTS

We acknowledge the financial support of the projects APVV-18-0480, APVV-17-0352, APVV-17-0560, APVV-16-0319, APVV-15-0641, APVV-15-0693, APVV-14-0745, SK-CN-RD-18-0006, VEGA 2/0092/18, VEGA 2/0149/17, ITMS 26230120002, ITMS 26210120002, DAAD/SAV grant, SERC Grant No. 152-70-00012, and the funding by the DFG. This work was performed during the implementation of the project Building-up Centre for Advanced Materials Application of the Slovak Academy of Sciences, ITMS Project Code 313021T081, supported by the Research & Innovation Operational Programme funded by the ERDF. We further acknowledge the Alexander von Humboldt foundation for the financial support of M.H.

REFERENCES

- (1) Nisato, G.; Lupo, D.; Ganz, S. *Organic and Printed Electronics: Fundamentals and Applications*; Jenny Stanford Publishing, 2016.
- (2) Brütting, W.; Adachi, C. *Physics of Organic Semiconductors*, 2nd ed.; Wiley, 2012.
- (3) Nalwa, H. S. *Conductive Polymers: Spectroscopy and Physical Properties*; Wiley, 1997; Vol. 3.
- (4) Werzer, O.; Baumgartner, R.; Zawodzki, M.; Roblegg, E. Particular Film Formation of Phenytoin at Silica Surfaces. *Mol. Pharmaceutics* **2014**, *11*, 610–616.
- (5) Christian, P.; Röthel, C.; Tazreiter, M.; Zimmer, A.; Salzmann, I.; Resel, R.; Werzer, O. Crystallization of Carbamazepine in Proximity to Its Precursor Iminostilbene and a Silica Surface. *Cryst. Growth Des.* **2016**, *16*, 2771–2778.
- (6) Tonazzini, I.; Bystrenova, E.; Chelli, B.; Greco, P.; Stolar, P.; Calò, A.; Lazar, A.; Borgatti, F.; D'Angelo, P.; Martini, C.; Biscarini, F. Multiscale Morphology of Organic Semiconductor Thin Films Controls the Adhesion and Viability of Human Neural Cells. *Biophys. J.* **2010**, *98*, 2804–2812.
- (7) Ciccoira, F.; Santato, C.; Dinelli, F.; Murgia, M.; Loi, M. A.; Biscarini, F.; Zamboni, R.; Heremans, P.; Muccini, M. Correlation between Morphology and Field-Effect-Transistor Mobility in Tetracene Thin Films. *Adv. Funct. Mater.* **2005**, *15*, 375–380.
- (8) Dimitrakopoulos, C. D.; Malenfant, P. R. L. Organic Thin Film Transistors for Large Area Electronics. *Adv. Mater.* **2002**, *14*, 99–117.
- (9) Jo, S. B.; Kim, H. H.; Lee, H.; Kang, B.; Lee, S.; Sim, M.; Kim, M.; Lee, W. H.; Cho, K. Boosting Photon Harvesting in Organic Solar Cells with Highly Oriented Molecular Crystals via Graphene–Organic Heterointerface. *ACS Nano* **2015**, *9*, 8206–8219.
- (10) Schünemann, C.; Wynands, D.; Eichhorn, K. J.; Stamm, M.; Leo, K.; Riede, M. Evaluation and Control of the Orientation of Small Molecules for Strongly Absorbing Organic Thin Films. *J. Phys. Chem. C* **2013**, *117*, 11600–11609.
- (11) Heinemeyer, U.; Broch, K.; Hinderhofer, A.; Kytka, M.; Scholz, R.; Gerlach, A.; Schreiber, F. Real-Time Changes in the Optical Spectrum of Organic Semiconducting Films and Their Thickness Regimes during Growth. *Phys. Rev. Lett.* **2010**, *104*, 257401.
- (12) Kytka, M.; Gerlach, A.; Schreiber, F.; Kováč, J. Real-Time Observation of Oxidation and Photo-Oxidation of Rubrene Thin

Films by Spectroscopic Ellipsometry. *Appl. Phys. Lett.* **2007**, *90*, 131911.

(13) Kowarik, S.; Gerlach, A.; Sellner, S.; Schreiber, F.; Cavalcanti, L.; Konovalov, O. Real-Time Observation of Structural and Orientational Transitions during Growth of Organic Thin Films. *Phys. Rev. Lett.* **2006**, *96*, 125504.

(14) Mayer, A. C.; Kazimirov, A.; Malliaras, G. G. Dynamics of Bimodal Growth in Pentacene Thin Films. *Phys. Rev. Lett.* **2006**, *97*, 105503.

(15) Burke, S. A.; Ji, W.; Mativetsky, J. M.; Topple, J. M.; Fostner, S.; Gao, H. J.; Guo, H.; Grütter, P. Strain Induced Dewetting of a Molecular System: Bimodal Growth of PTCDA on NaCl. *Phys. Rev. Lett.* **2008**, *100*, 7–10.

(16) Schreiber, F. Organic Molecular Beam Deposition: Growth Studies beyond the First Monolayer. *Physica Status Solidi (A) Applied Research* **2004**, *201*, 1037–1054.

(17) Witte, G.; Wöll, C. Growth of Aromatic Molecules on Solid Substrates for Applications in Organic Electronics. *J. Mater. Res.* **2004**, *19*, 1889–1916.

(18) Klopotek, M.; Hansen-Goos, H.; Dixit, M.; Schilling, T.; Schreiber, F.; Oettel, M. Monolayers of Hard Rods on Planar Substrates. II. Growth. *J. Chem. Phys.* **2017**, *146*, 084903.

(19) Hagara, J.; Mrkyvkova Tesarova, N.; Nadazdy, P.; Hodas, M.; Bodik, M.; Jergel, M.; Majkova, E.; Tokár, K.; Hutar, P.; Sojkova, M.; Chumakov, A.; Konovalov, O.; Pandit, P.; Roth, S. V.; Hinderhofer, A.; Hulman, M.; Siffalovic, P.; Schreiber, F. Reorientation of π -Conjugated Molecules on Few-Layer MoS₂ Films. *Phys. Chem. Chem. Phys.* **2020**, 223097.

(20) Huang, H.; Huang, Y.; Wang, S.; Zhu, M.; Xie, H.; Zhang, L.; Zheng, X.; Xie, Q.; Niu, D.; Gao, Y. Van Der Waals Heterostructures between Small Organic Molecules and Layered Substrates. *Crystals* **2016**, *6*, 113.

(21) Zhang, L.; Roy, S. S.; Safron, N. S.; Shearer, M. J.; Jacobberger, R. M.; Saraswat, V.; Hamers, R. J.; Arnold, M. S.; Andrew, T. L. Orientation Control of Selected Organic Semiconductor Crystals Achieved by Monolayer Graphene Templates. *Adv. Mater. Interfaces* **2016**, *3*, 1600621.

(22) Hlawacek, G.; Khokhar, F. S.; van Gestel, R.; Zandvliet, H. J. W.; Poelsema, B.; Teichert, C. In-Situ Observation of Organic Thin Film Growth on Graphene. *Springer Ser. Mater. Sci.* **2013**, *173*, 107–139.

(23) Lüth, H. *Solid Surfaces, Interfaces and Thin Films*; Graduate Texts in Physics; Springer International Publishing: Cham, 2015.

(24) Hexemer, A.; Müller-Buschbaum, P. Advanced Grazing-Incidence Techniques for Modern Soft-Matter Materials Analysis. *IUCrJ* **2015**, *2*, 106–125.

(25) Norris, A. C. Monitoring Growth with X-Ray Diffraction Monitoring Growth with X-Ray Diffraction. *Philos. Trans. Phys. Sci. Eng.* **1993**, *344*, 557–566.

(26) Kowarik, S.; Gerlach, A.; Schreiber, F. Organic Molecular Beam Deposition: Fundamentals, Growth Dynamics, and in Situ Studies. *J. Phys.: Condens. Matter* **2008**, *20*, 184005.

(27) Bommel, S.; Kleppmann, N.; Weber, C.; Spranger, H.; Schäfer, P.; Novak, J.; Roth, S. V.; Schreiber, F.; Klapp, S. H. L.; Kowarik, S. Unravelling the Multilayer Growth of the Fullerene C 60 in Real Time. *Nat. Commun.* **2014**, *5*, 1–8.

(28) Ezquerro, T. A.; Garcia-Gutierrez, M.; Nogales, A.; Gomez, M. *Applications of Synchrotron Light to Scattering and Diffraction in Materials and Life Sciences*; Springer, 2009.

(29) Rauscher, M.; Paniago, R.; Metzger, H.; Kovats, Z.; Domke, J.; Peisl, J.; Pfannes, H.-D.; Schulze, J.; Eisele, I. Grazing Incidence Small Angle X-Ray Scattering from Free-Standing Nanostructures. *J. Appl. Phys.* **1999**, *86*, 6763–6769.

(30) Renaud, G.; Lazzari, R.; Leroy, F. Probing Surface and Interface Morphology with Grazing Incidence Small Angle X-Ray Scattering. *Surf. Sci. Rep.* **2009**, *64*, 255–380.

(31) Holý, V.; Pietsch, U.; Baumbach, T. *High-Resolution X-Ray Scattering from Thin Films and Multilayers*; Springer, 1999.

- (32) Breiby, D. W.; Bunk, O.; Andreasen, J. W.; Lemke, H. T.; Nielsen, M. M. Simulating X-Ray Diffraction of Textured Films. *J. Appl. Crystallogr.* **2008**, *41*, 262–271.
- (33) Resel, R.; Bainschab, M.; Pichler, A.; Dingemans, T.; Simbrunner, C.; Stangl, J.; Salzmänn, I. Multiple Scattering in Grazing-Incidence X-Ray Diffraction: Impact on Lattice-Constant Determination in Thin Films. *J. Synchrotron Radiat.* **2016**, *23*, 729–734.
- (34) Mrkyvkova, N.; Hodas, M.; Hagara, J.; Nadazdy, P.; Halahovets, Y.; Bodik, M.; Tokar, K.; Chai, J. W.; Wang, S. J.; Chi, D. Z.; Chumakov, A.; Konovalov, O.; Hinderhofer, A.; Jergel, M.; Majkova, E.; Siffalovic, P.; Schreiber, F. Diindenoperylene Thin-Film Structure on MoS₂ Monolayer. *Appl. Phys. Lett.* **2019**, *114*, 251906.
- (35) Li, H.; Zhang, Q.; Yap, C. C. R.; Tay, B. K.; Edwin, T. H. T.; Olivier, A.; Baillargeat, D. From Bulk to Monolayer MoS₂: Evolution of Raman Scattering. *Adv. Funct. Mater.* **2012**, *22*, 1385–1390.
- (36) Sojková, M.; Siffalovic, P.; Babchenko, O.; Vanko, G.; Dobročka, E.; Hagara, J.; Mrkyvkova, N.; Majková, E.; Ižák, T.; Kromka, A.; Hulman, M. Carbide-Free One-Zone Sulfurization Method Grows Thin MoS₂ Layers on Polycrystalline CVD Diamond. *Sci. Rep.* **2019**, *9*, 2001.
- (37) Ritley, K. A.; Krause, B.; Schreiber, F.; Dosch, H. A Portable Ultrahigh Vacuum Organic Molecular Beam Deposition System for in Situ X-Ray Diffraction Measurements. *Rev. Sci. Instrum.* **2001**, *72*, 1453–1457.
- (38) Yoneda, Y. Anomalous Surface Reflection of X Rays. *Phys. Rev.* **1963**, *131*, 2010–2013.
- (39) Dürr, A. C.; Schreiber, F.; Münch, M.; Karl, N.; Krause, B.; Kruppa, V.; Dosch, H. High Structural Order in Thin Films of the Organic Semiconductor Diindenoperylene. *Appl. Phys. Lett.* **2002**, *81*, 2276–2278.
- (40) Dürr, A. C.; Koch, N.; Kelsch, M.; Ruhm, A.; Ghijsen, J.; Johnson, R. L.; Pireaux, J.-J.; Schwartz, J.; Schreiber, F.; Dosch, H.; Kahn, A. Interplay between Morphology, Structure, and Electronic Properties at Diindenoperylene-Gold Interfaces. *Phys. Rev. B: Condens. Matter Mater. Phys.* **2003**, *68*, 115428.
- (41) Stein, G. E.; Kramer, E. J.; Li, X.; Wang, J. Layering Transitions in Thin Films of Spherical-Domain Block Copolymers. *Macromolecules* **2007**, *40*, 2453–2460.
- (42) Pithan, L.; Nabok, D.; Cocchi, C.; Beyer, P.; Duva, G.; Simbrunner, J.; Rawle, J.; Nicklin, C.; Schäfer, P.; Draxl, C.; Schreiber, F.; Kowarik, S. Molecular Structure of the Substrate-Induced Thin-Film Phase of Tetracene. *J. Chem. Phys.* **2018**, *149*, 144701.
- (43) Jones, A. O. F.; Röthel, C.; Lassnig, R.; Bedoya-Martínez, O. N.; Christian, P.; Salzmänn, I.; Kunert, B.; Winkler, A.; Resel, R. Solution of an Elusive Pigment Crystal Structure from a Thin Film: A Combined X-Ray Diffraction and Computational Study. *CrystEngComm* **2017**, *19*, 1902–1911.
- (44) Kowarik, S.; Gerlach, A.; Sellner, S.; Cavalcanti, L.; Konovalov, O.; Schreiber, F. Real-Time X-Ray Diffraction Measurements of Structural Dynamics and Polymorphism in Diindenoperylene Growth. *Appl. Phys. A: Mater. Sci. Process.* **2009**, *95*, 233–239.
- (45) Als-Nielsen, J.; McMorrow, D. *Elements of Modern X-Ray Physics*, 2nd ed.; Wiley, 2011.
- (46) Birkholz, M. *Thin Film Analysis by X-Ray Scattering*; Wiley, 2006.
- (47) Kratzer, M.; Teichert, C. Thin Film Growth of Aromatic Rod-like Molecules on Graphene. *Nanotechnology* **2016**, *27*, 292001.
- (48) Matković, A.; Genser, J.; Lüftner, D.; Kratzer, M.; Gajić, R.; Puschnig, P.; Teichert, C. Epitaxy of Highly Ordered Organic Semiconductor Crystallite Networks Supported by Hexagonal Boron Nitride. *Sci. Rep.* **2016**, *6*, 38519.
- (49) Hodas, M.; Siffalovic, P.; Nádaždy, P.; Mrkyvková, N.; Bodik, M.; Halahovets, Y.; Duva, G.; Reisz, B.; Konovalov, O.; Ohm, W.; Jergel, M.; Majková, E.; Gerlach, A.; Hinderhofer, A.; Schreiber, F. Real-Time Monitoring of Growth and Orientational Alignment of Pentacene on Epitaxial Graphene for Organic Electronics. *ACS Appl. Nano Mater.* **2018**, *1*, 2819–2826.
- (50) Czajkowski, K. M.; Świtlik, D.; Langhammer, C.; Antosiewicz, T. J. Effective Optical Properties of Inhomogeneously Distributed Nanoobjects in Strong Field Gradients of Nanoplasmonic Sensors. *Plasmonics* **2018**, *13*, 2423–2434.
- (51) Oura, K.; Katayama, M.; Zotov, A. V.; Lifshits, V. G.; Saranin, A. A. *Growth of Thin Films*; Springer: Berlin, Heidelberg, 2003.